Hindawi Publishing Corporation
Journal of Nanomaterials
Volume 2016, Article ID 4592501, 12 pages
http://dx.doi.org/10.1155/2016/4592501

*Research Article*

# Effect of Frequency on Pulsed Fluidized Beds of Ultrafine Powders

**Syed Sadiq Ali,[1] Ebrahim H. Al-Ghurabi,[2] Abdelhamid Ajbar,[2] Yahya A. Mohammed,[3] Mourad Boumaza,[2] and Mohammad Asif[2]**

[1]*Department of Chemical Engineering, King Faisal University, P.O. Box 380, Al-Ahsa 31982, Saudi Arabia*
[2]*Department of Chemical Engineering, King Saud University, P.O. Box 800, Riyadh 11421, Saudi Arabia*
[3]*King Saud University, P.O. Box 800, Riyadh 11421, Saudi Arabia*

Correspondence should be addressed to Mohammad Asif; masif@ksu.edu.sa

Received 21 October 2015; Revised 17 January 2016; Accepted 18 January 2016

Academic Editor: Takuya Tsuzuki



Deagglomeration of ultrafine powders poses an important challenge towards their efficient and effective utilization. In the present study, we investigate the effect of frequency on the hydrodynamics of pulsed fluidized beds of ultrafine powders that show strong agglomeration behavior. We have carefully selected square waves of three different frequencies: 0.05 Hz, 0.10 Hz, and 0.25 Hz. The lowest frequency used here allowed the fluidized bed to settle completely before another pulse was introduced whilst the highest frequency ensured that the bed remained in a state of continuous turbulence between occurrences of consecutive pulses. On the other hand, the intermediate frequency pulse was just sufficient to complete the process of bed collapse before the start of the next pulse. Both local and global bed dynamics in all the three cases were rigorously monitored using fast response pressure transducers. The pressure transient data during the bed collapse were processed using the bed collapse model reported in the literature to compute the effective hydrodynamic diameter of agglomerates. Though there was substantial decrease in the agglomerate size, the effect of the frequency appeared to be rather insignificant as the global pressure transients remained rather insensitive to the change of the fluidization velocity.

## 1. Introduction

Due to strong interparticle van der Waals forces, ultrafine powders tend to agglomerate. The size of agglomerates can sometimes reach several orders of magnitude larger than the primary particle size of the powder. The phenomenon of agglomeration severely compromises the effectiveness of nanopowders, thus necessitating the use of techniques that can help promote their deagglomeration. Pulsed fluidized beds have lately attracted a lot of attention towards this end. This belongs to a class of assisted fluidization techniques, whereby the fluidized bed technology is further assisted with a technique to improve the fluidization quality, enhance the bed homogeneity, and promote the deagglomeration [1–4]. The choice of a suitable assisted fluidization technique in an actual application is nevertheless governed by several issues, for example, energy usage, contamination concerns, and scale-up challenges. When evaluated on the basis of these factors, pulsed fluidized beds hold greater promise as compared to other assisted fluidization techniques. For example, pulsed fluidization substantially reduced the energy requirement during the drying of sodium acetate as the flow pulsation helped to break agglomerates and provided better contact between particles and gas [5]. Pulsed fluidized beds have also been used to improve the drying of porous pharmaceutical granules, agricultural products, and cohesive granules of polyhydroxybutyrate (PHB) [6–8]. Due to flow pulsation, a faster and homogeneous drying was invariably reported in most applications owing to better heat and mass transfer rates. Akhavan et al. used pulsed fluidized bed to enhance the fluidization quality and lower channeling and plugging problems often encountered with cohesive powders of nanoparticles [1, 9]. Other recent applications of pulsed fluidized beds include efficient degradation of toxic chemical

(carbamazepine) by *Trametes versicolor* using the pulsation of inlet flow of the air [10].

Despite a wide range of potential applications, studies concerning hydrodynamic aspects of pulsed fluidized beds appear to be relatively scarce. A recent study by Khosravi Bizhaem and Basirat Tabrizi using high speed camera confirmed the efficacy of flow pulsation in improving the fluidization hydrodynamics of micro-sized solid particles [11]. For the case of 95 $\mu$m Alumina particles (Geldart Group A/B), both the bubble diameter and the bed expansion decreased whereas the bed pressure drop increased with the increase in the pulsation frequency. For the case of fine cohesive powders (Group C) consisting of 20 $\mu$m Alumina particles, only high frequency flow pulsation could achieve fluidization. Ali and Asif used pulsed fluidized bed to improve the fluidization behavior of ultrafine hydrophilic nanopowder that showed strong agglomeration behavior [12]. There was a significant decrease in the minimum fluidization velocity which was obtained from the measurement of the local pressure drop. Using the minimum fluidization velocity data and the overall bed void fraction, the effective diameter of the nanopowder present in the bed was computed. A substantial reduction in the average particle size was obtained due to the flow pulsation. However, no clear effect of the pulse frequency on the minimum fluidization velocity was noticeable in their study. On the other hand, for the case of hydrophobic nanopowder (Aerosil R974), Akhavan et al. [1] reported almost 30% decrease in the minimum fluidization velocity when the pulsation frequency was increased fivefold from 1 Hz to 5 Hz. The effect of frequency on other ultrafine nanopowders was not reported in their study. Recently, Liu et al. pointed out that bed collapse experiments can give valuable insight into the fluidization behavior [2]. Their experimental minimum fluidization velocity for a superfine powder was found to be much higher than the corresponding theoretical value. They concluded that the fluidization behavior of superfine particles is similar to nanoparticles. In a recent study, Ali et al., instead of monitoring the bed height like most previous studies, recorded global pressure transient data to analyze the collapse dynamics of pulsed fluidized bed [13]. The pulsation frequency in their study was kept fixed at 0.1 Hz. From the collapse data, authors computed the effective terminal velocity of the powder using the model of Nie and Liu in conjunction with the Richardson-Zaki correlation [14]. As compared to the mean diameter obtained using particle size analyzer, there was almost 40% decrease in the diameter of the particles. The effect of the air velocity was however found to be negligible in their study.

The focus of the present study is to investigate the effect of the pulsation frequency on the hydrodynamics of pulsed fluidized beds containing hydrophilic nanoparticles that show strong agglomeration behavior during their contacting with the gas phase. Three different frequencies, that is, 0.05 Hz, 0.10 Hz, and 0.25 Hz, were carefully selected for pulsating the inlet air flow. For the low frequency pulsation (0.05 Hz), the time was more than sufficient for the bed to attain steady state before the next step change in the inlet air was introduced by either opening or closing the air supply. For 0.1 Hz pulsation, the pulse duration of 5 seconds was just sufficient to allow the whole bed to attain steady state before the next velocity step change. When the flow pulsation was fixed at 0.25 Hz, the pulsed fluidized bed was never able to attain a steady state. Due to short pulses in this case, neither the bed expansion nor the collapse process was complete before the next pulse occurred. In all cases, both local and global response of the bed were carefully monitored using fast response pressure transducers in order to characterize the bed hydrodynamics. Extending our earlier work [12] that used local pressure transients to determine the minimum fluidization velocities, global pressure transient data are processed here for the three different cases of pulsation frequencies in conjunction with the bed collapse model of Nie and Liu to obtain the effective hydrodynamic diameter of nanopowder present in the bed [14].

## 2. Mathematical Model

The salient features of the three-region model of the bed collapse process, proposed by Nie and Liu, are briefly discussed in the following section [14]. The solid balance approach is followed here for describing interface transients, though the same results can also be obtained using the interfacial fluid balance approach as discussed in the Appendix.

The model schematic delineating three different regions is shown in Figure 1. The lower region (Region 1) of height $L_1$ is located immediately above the distributor and is mainly composed of settled solids and thus resembles a packed bed. Region 2 on the other hand is free of gas bubbles while Region 3 consists of three phases, which are emulsion phase, bubbles, and wakes. As the collapse process proceeds, the upper two regions, after the escape of gas bubbles, coalesce as seen in Figure 1(b). The end of the collapse process is marked with the complete settling of bed as shown in Figure 1(c). The main assumptions of the model are as follows:

(1) Velocities of bubbles and wakes trailing the bubbles in Region 3 are the same.

(2) Compositions of the wake and emulsion phase in Regions 3 are the same.

(3) Emulsion phase composition in both Region 3 and Region 2 is the same.

(4) There are constant gas physical fluid properties along bed height.

(5) Particle fraction in Region 1 is constant throughout the collapse process.

For the interface located at $L_1$, the solid balance leads to

$$C_{S_1}\left(U_{S_1} - \frac{dL_1}{dt}\right) = C_{S_2}\left(U_{S_2} - \frac{dL_1}{dt}\right), \tag{1}$$

where $C_S$ denotes solid fraction and $U_S$ is its velocity. Rearranging,

$$\left(C_{S_1} - C_{S_2}\right)\frac{dL_1}{dt} = C_{S_1}U_{S_1} - C_{S_2}U_{S_2}. \tag{2}$$

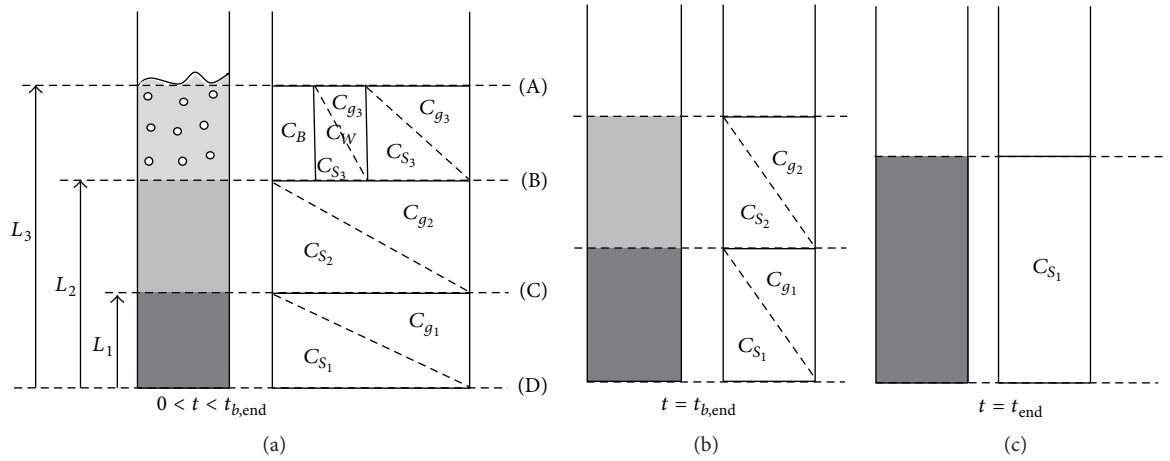


Figure 1: Schematic representation of the bed collapse process.

During the process of the bed collapse, the bed region immediately above the distributor possesses zero solid velocity; that is, $U_{S_1} = 0$, and the solid concentration in the lower bed region is constant. Therefore,

$$\left(C_{S_1} - C_{S_2}\right)\frac{dL_1}{dt} = -C_{S_2}U_{S_2}. \tag{3}$$

Since, for Region 2,

$$C_{S_2}U_{S_2} + C_{g_2}U_{g_2} = U_{g_0}, \tag{4}$$

where $U_{g_0}$ is the air superficial velocity, therefore,

$$U_{S_2} = U_{g_0} - C_{g_2}U_{r_2} = U_{g_0} - \left(1 - C_{S_2}\right)U_{r_2}. \tag{5}$$

If the solid concentration is assumed to be constant, so will be the relative velocity owing to its dependence on the solid concentration and its terminal velocity. Hence, the time dependence of the lower interface is given by

$$L_1 = -\left[\frac{\left(U_{g_0} - \left(1 - C_{S_2}\right)U_{r_2}\right)C_{S_2}}{\left(C_{S_1} - C_{S_2}\right)}\right]t. \tag{6}$$

For the interface located at $L_2$, the solid balance leads to

$$\begin{aligned} C_{S_2}\left(U_{S_2} - \frac{dL_2}{dt}\right) &= C_{S_3}C_E\left(U_{S_3} - \frac{dL_2}{dt}\right) \\ &\quad + C_{S_3}C_W\left(U_W - \frac{dL_2}{dt}\right), \end{aligned} \tag{7}$$

where $C_B$, $C_E$, and $C_W$ are volumetric fractions of bubbles, emulsion phase, and wakes, respectively, in the region between $L_2$ and $L_3$ whereas $U_B$, $U_E$, and $U_W$ are their respective velocities. Note that bubbles are comprised of gas phase only while wakes consist of both gas and solid phases. It is moreover assumed here that fractions of two phases, that is, solid and gas, are the same in both emulsion phase and the wakes trailing the gas bubbles (Assumption 2). Since

$$C_B + C_E + C_W = 1, \tag{8}$$

equation (7) can therefore be simplified and rearranged as

$$\left(\frac{C_{S_2}}{C_{S_3}} - \left(1 - C_B\right)\right)\frac{dL_2}{dt} = \frac{C_{S_2}}{C_{S_3}}U_{S_2} - C_EU_{S_3} - C_WU_W. \tag{9}$$

From continuity considerations for Region 3,

$$\begin{aligned} C_BU_B + C_WU_W + C_EU_E &= U_{g_0}, \\ U_E = C_{g_3}U_{g_3} + C_{S_3}U_{S_3} &= U_{S_3} + C_{g_3}U_{r_3}. \end{aligned} \tag{10}$$

Further, the velocity of wake following the bubble is the same as bubbles; that is, $U_B = U_W$ (Assumption 1) and $C_{S_2} = C_{S_3}$ (Assumption 3). Therefore, (9) can also be written in terms of relative velocities as follows:

$$C_B\frac{dL_2}{dt} = C_EC_{g_3}U_{r_3} - C_{g_2}U_{r_2} + C_BU_B. \tag{11}$$

Integrating,

$$L_2 = \left[\frac{\left\{C_BU_B + C_{g_2}\left(C_EU_{r_3} - U_{r_2}\right)\right\}}{C_B}\right]t. \tag{12}$$

One can similarly write for surface located at $L_3$

$$\begin{aligned} &C_{S_3}C_E\left(U_{S_3} - \frac{dL_3}{dt}\right) + C_{S_3}C_W\left(U_W - \frac{dL_3}{dt}\right) \\ &\quad = C_{S_4}\left(U_{S_4} - \frac{dL_3}{dt}\right). \end{aligned} \tag{13}$$

Since $L_3$ is the top fluidized bed interface,

$$\begin{aligned} C_{S_4} &= 0, \\ U_{S_4} &= 0. \end{aligned} \tag{14}$$

Simplifying and rearranging (11) gives

$$\left(1 - C_B\right)\frac{dL_3}{dt} = C_EU_{S_3} + C_WU_W. \tag{15}$$

If the fraction of wakes is assumed to be zero, the above equation reduces to

$$\frac{dL_3}{dt} = U_{S_3} \tag{16}$$

two-region model. Equation (15) can also be written, in terms of relative velocity, as follows:

$$\left(1 - C_B\right)\frac{dL_3}{dt} = U_{g_0} - C_E C_{g_3} U_{r_3} - C_B U_B. \tag{17}$$

Integrating,

$$L_3 = L_0 + \left[\frac{U_{g_0} - C_B U_B - C_E C_{g_3} U_{r_3}}{\left(1 - C_B\right)}\right] t. \tag{18}$$

In the present work, the transients of the total pressure drop across the pulsed fluidized bed are measured. It is therefore important that the interface transients presented in equations above are correlated with the pressure drop transients. Since the total pressure drop for the fluidized bed is the sum of contributions of each region, that is,

$$\begin{aligned}(-\Delta P) = &\int_0^{L_1}\left(-\frac{dP_1}{dx}\right)dx + \int_{L_1}^{L_2}\left(-\frac{dP_2}{dx}\right)dx \\ &+ \int_{L_2}^{L_3}\left(-\frac{dP_3}{dx}\right)dx\end{aligned} \tag{19}$$

or

$$\begin{aligned}(-\Delta P) = &\int_0^{L_1}\left(-\Delta p_1\right)dx + \int_{L_1}^{L_2}\left(-\Delta p_2\right)dx \\ &+ \int_{L_2}^{L_3}\left(-\Delta p_3\right)dx,\end{aligned} \tag{20}$$

where $\Delta p_i$ is the pressure gradient and equal to the bed weight in fluidized bed, therefore, the above equation can be written as

$$\begin{aligned}(-\Delta P) = &\int_0^{L_1}\left(-\Delta p_1\right)dx + \int_{L_1}^{L_2}\left(C_{S_2}\rho_s g\right)dx \\ &+ \int_{L_2}^{L_3}\left(C_{S_3}\left(C_E + C_W\right)\rho_s g\right)dx\end{aligned} \tag{21}$$

or

$$\begin{aligned}(-\Delta P) = &\left(-\Delta p_1\right)L_1 + \left(C_{S_2}\right)\left(L_2 - L_1\right)\rho_s g \\ &+ \left(C_{S_3}\right)\left(C_E + C_W\right)\left(L_3 - L_2\right)\rho_s g.\end{aligned} \tag{22}$$

The pressure drop in Region 1 can be evaluated using pressure drop correlations for the packed bed, which can be represented as follows:

$$\left(-\Delta p_1\right) = \alpha U_{g_0}, \tag{23}$$

where the constant ($\alpha$) for the case of commonly used Kozney-Carman correlation for the pressure drop in laminar flow regime can be expressed as

$$\alpha = \frac{180\mu C_{S_1}^2}{{d_P}^2 C_{g_1}^3}. \tag{24}$$

It was shown by Ali et al. [13] that the total pressure drop, after simplification, can be represented as

$$(-\Delta P) = \beta t + \gamma, \tag{25}$$

where

$$\begin{aligned}\beta &= -\frac{\left(U_{g_0} - \left(1 - C_{S_2}\right)U_r\right)\left(\alpha U_{g_0} - C_{S_2}\rho_p g\right)C_{S_2}}{\left(C_{S_1} - C_{S_2}\right)}, \\ \gamma &= L_0\left(1 - C_B\right)C_{S_3}\rho_p g.\end{aligned} \tag{26}$$

The relative velocity in the above expression can be evaluated using the Richardson-Zaki correlation for the Stokes law regime as follows [15]:

$$U_r = U_t\left(1 - C_S\right)^{4.8}, \tag{27}$$

where the particle terminal velocity ($U_t$) in the Stokes law regime is given by [16]

$$U_t = \frac{\left(\rho_p - \rho_f\right)g{d_P}^2}{18\mu}, \tag{28}$$

where $\rho_p$ is the solid density and $\rho_f$ and $\mu$ are the air density and viscosity, respectively. Thus, once the value of the $U_t$ is known, the hydrodynamic diameter ($d_P$) of particles can be determined.

## 3. Experimental

Details of the experimental setup are explained elsewhere [12]. The key features of the present experiments are nonetheless briefly presented here. The test section was a 1.5 m long transparent Perspex column of 70 mm internal diameter preceded by a 0.5 m long calming section of the same diameter. A 12 mm thick perforated plate with 2 mm hole on a square pitch and 4% open area acted as distributor separating the two sections.

Hydrophobic fumed silica, with a primary size of 12 nm and surface area of 200 $m^2$/g, was used as the fluidized mass. Its dry size analysis however yields a wide size distribution that ranges from 2 $\mu$m to 100 $\mu$m with an average size of approximately 20 $\mu$m owing to the phenomenon of agglomeration [12]. The bulk density of the sample was very low (50 kg/$m^3$) as compared to its true solid density (2200 kg/$m^3$). Therefore, the porosity of the ultrafine powder was over 0.97, which is an exceptionally high value not normally encountered for micro- or macro-sized solids. The high porosity of the present nanopowder can be attributed to several levels of agglomeration due to the interparticle van der Waals forces.

Compressed ambient air was used as the fluidizing medium here. Gilmont flowmeter of range 5.0–87.5 LPM was used to control the air flow that was measured using the flow totalizer (Omega model FMA 1611) connected to the data acquisition system (NI USB-6289).

The flow pulsation was generated using a solenoid valve. The open position of the valve allowed the passage of the air

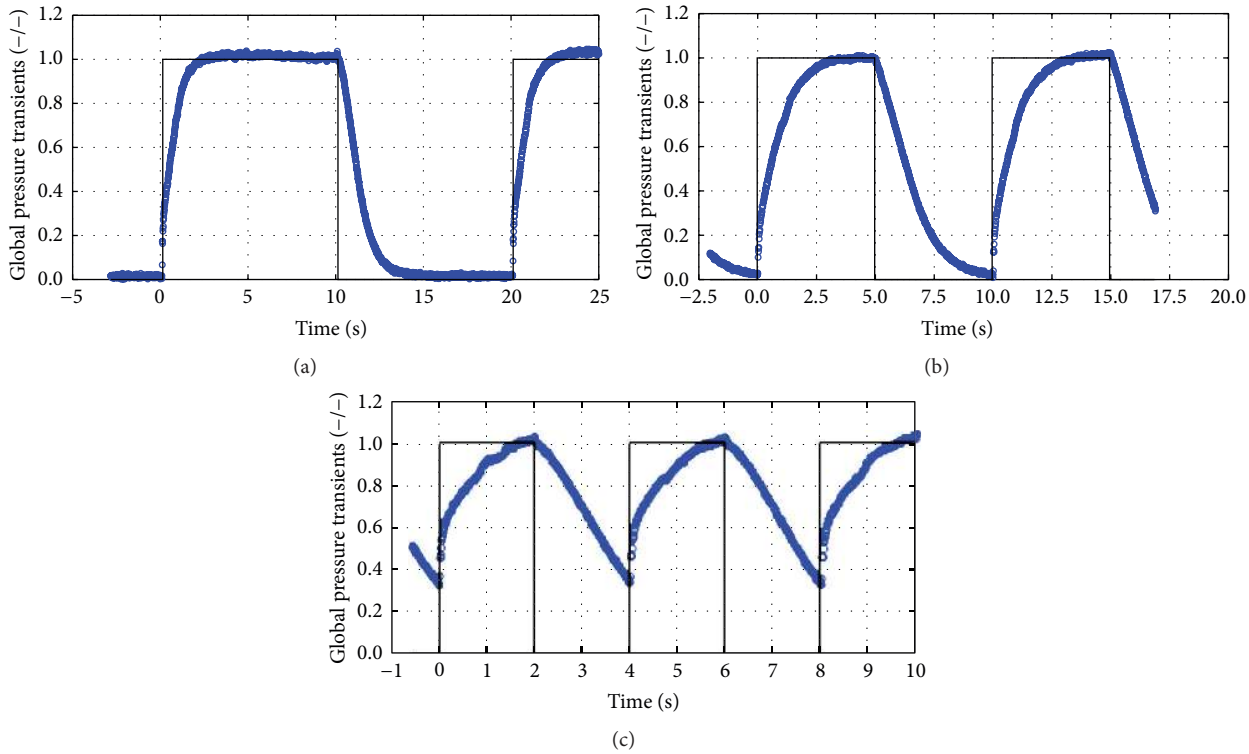


Figure 2: Global pressure transients at 134.8 mm/s for pulsed fluidized bed at frequencies: (a) 0.05 Hz, (b) 0.10 Hz, and (c) 0.25 Hz.

through the test section of the column at a preset flow rate while the closed position of the valve stopped the air flow thus initiating the process of the bed collapse. The opening and closing of the valve were precisely controlled with the help of data acquisition system (DAQ) connected to a laptop running Labview software.

The local and global pressure drops in the test section of the fluidized bed were measured using fast response pressure transducers with a response time of 1 millisecond. The local pressure drop was measured using bidirectional differential pressure transducer (Omega PX163-005BD5V) with its taps, flush with the column wall, located at a distance of 110 mm and 230 mm above the distributor. On the other hand, the global pressure drop was monitored using another fast response pressure transducer (Omega PX163-005BD10V) which has one tap located just above the distributor while the other tap was open to the atmosphere in order to record the overall pressure drop of the fluidized bed. The pressure transient data were recorded at a sampling frequency of 100 samples per second using data acquisition system.

The study involved generation of square pulses of three different frequencies. First series of low frequency experiments involved 0.05 Hz pulses by keeping the solenoid valve open for 10 s and closed for the next 10 s. This process was repeated several times. Pressure transient data were recorded only after several pulses were carried out. A typical global transient response of the bed is shown in Figure 2(a). The pressure data were normalized with respect to the weight of the bed. The corresponding open and close positions of the valve are also plotted with thick dark lines. As seen in Figure 2(a), the bed immediately responds to the step change in flow and attains a steady state for a sufficiently long period of time during both open and close positions of the valve. The next velocity step change occurs only after bed transients have completely died out. Second series of experiments involved pulsed fluidized bed of 0.10 Hz frequency. The air flow through the bed was maintained for 5 s while the flow was stopped for the next 5 s. The duration of 5 s was barely sufficient to allow the bed to attain a steady state, as seen from the pressure transients in Figure 2(b), before the next velocity step change was introduced. The 0.25 Hz flow pulsation was carried out in the third series of experiments. In this case, the velocity step changes were made at a regular interval of 2 s. It can be seen in Figure 2(c) that the steady-state condition is not achieved during the 2 s pulse as the next pulse starts before the bed collapse process is complete. The response of the bed for each of the three frequencies discussed above was studied for a wide range of superficial velocities varying from 6 mm/s to 150 mm/s.

## 4. Results and Discussion

Both local and global bed transients are shown in Figure 3. The flow rate in this case is very small ($U_o$ = 6.28 mm/s) so that the bed is in packed state. As seen in Figure 3(a), the local pressure drop in the packed bed is only 10 Pa (approximately) when there is no flow pulsation. As the pulse starts, the pressure drop shows as much as eight- to tenfold increase. This sudden jump in the pressure is due to the impulse of the air entering the test section of the bed which is mainly

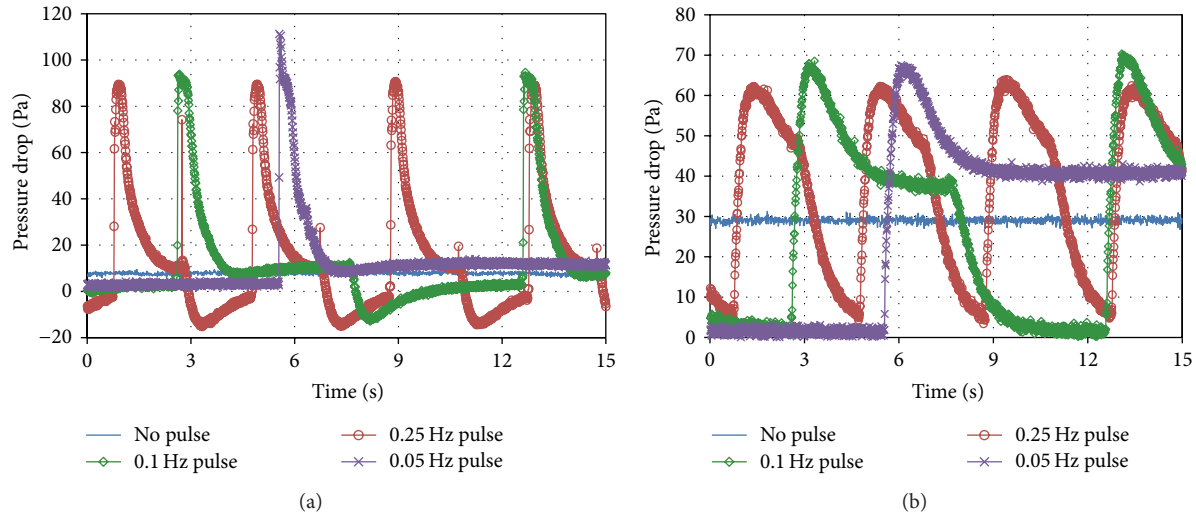


Figure 3: Pressure transients for different frequencies at 6.28 mm/s: (a) local pressure, (b) global pressure.

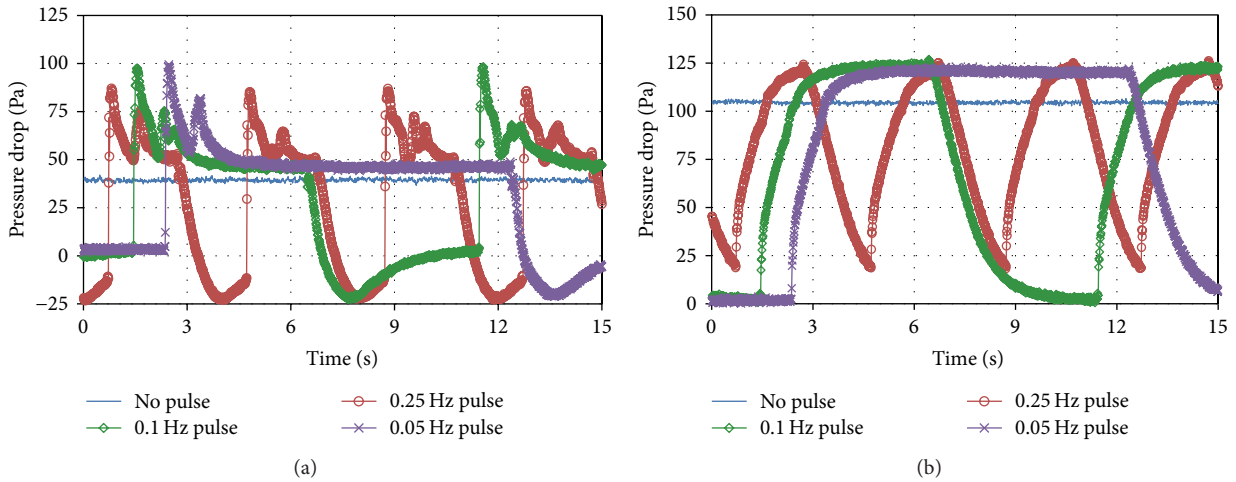


Figure 4: Pressure transients for different frequencies at 65.9 mm/s: (a) local pressure, (b) global pressure.

contributed by the pressure build-up in the line when the valve is closed. The case of the global pressure drop is shown in Figure 3(b) where the steady-state pressure drop is approximately 30 Pa while peak values are as much as 60 Pa due to flow pulsation. Thus, there is hardly a twofold increase in the peak value here as compared to tenfold increase seen before. Moreover, global transient profiles are much broader as compared to their local transient counterpart. This indicates that any disturbance that is introduced in the bed is quickly mitigated by the bed of solids as it travels through the bed. Therefore, the global response of the bed gets quite subdued as compared to the local response of the bed. The global pressure drop for the case of no pulse is seen to be lower than the steady-state pressure drop achieved after the valve closing for the pulse fluidized beds. This can be attributed to the lack of bed homogeneity due to the uneven expansion of the nanopowder when there was no pulsation through the test section of the column.

Figure 4 shows the case of a fully fluidized bed at the air superficial velocity of 65.9 mm/s. The local pressure transient profiles indicate occurrence of vigorous bed disturbances due to the flow pulsation. As far as effect of different frequencies is concerned, a greater turbulence is noticed for higher frequency beds as compared to ones for lower frequency. For example, there are only two distinct peaks for 10 s pulses whereas several smaller peaks are seen for 2 s pulsed flow. Since the air superficial velocity is higher than the minimum fluidization velocity, the bed settling under gravity during the closed position of the solenoid valve does not have enough time to settle completely for the case of high frequency pulses. The bed solids are subjected to next air pulse before coming to rest due to the opening of the solenoid valve. Hence, a greater degree of solid motion is seen with high frequency as compared to ones with lower frequency where the bed solids get more time to settle down and come to rest. Moreover, negative pressures are seen to occur when the bed collapse process starts after the flow interruption. This can be attributed to negative momentum acquired by solids during their fall under the gravity from heights attained during their fluidization. Another factor that can lead to this behavior is

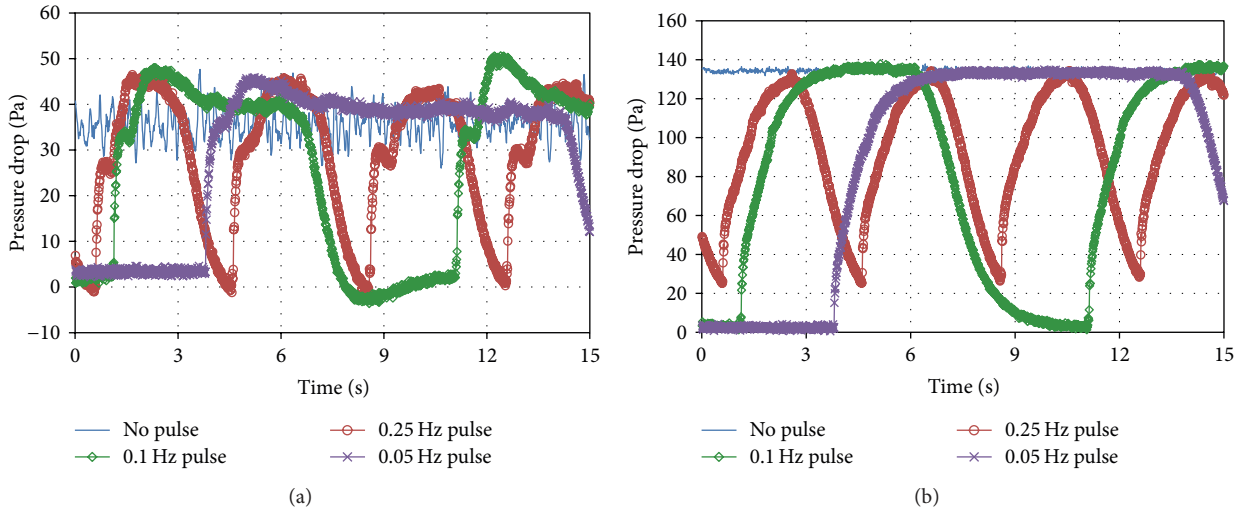


FIGURE 5: Pressure transients for different frequencies at 152.9 mm/s: (a) local pressure, (b) global pressure.

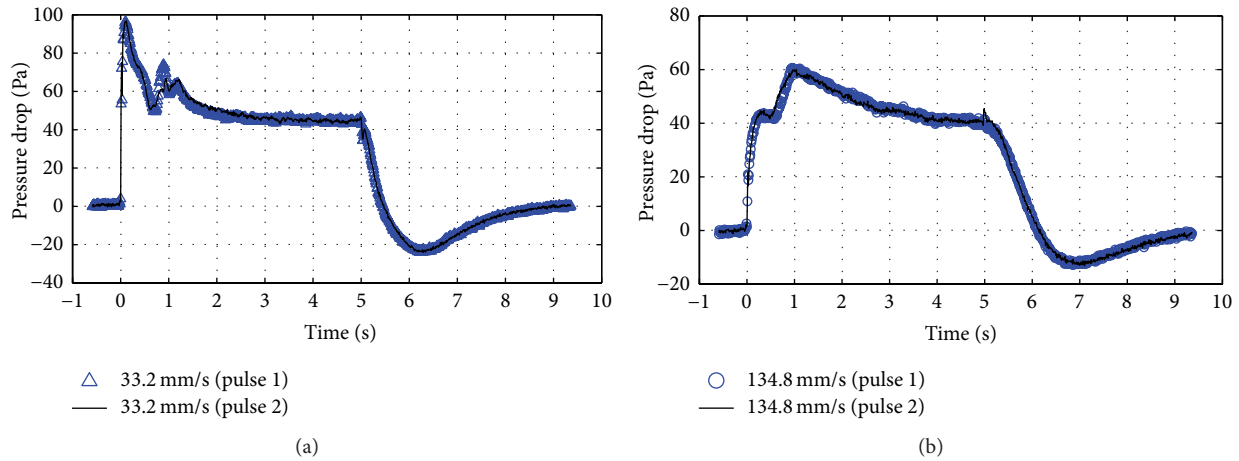


FIGURE 6: Local pressure transients for two consecutive pulses at 0.10 Hz at velocities: (a) 33.2 mm/s, (b) 134.8 mm/s.

the sudden lacunae in the air supply to the test section due to the flow interruption that causes the air present in the upper section of the column to flow backwards [17]. On the other hand, global pressure transients are quite smooth. It is also seen that bed collapse transients, irrespective of pulsation frequency, are quite comparable. It is also seen that overall bed is quite homogeneous for the case of flow pulsation as the global pressure drop during the air flow is the same in all the three cases of different pulse frequency while the corresponding value for the case of unassisted conventional fluidization is lower due probably to bed nonhomogeneities.

Figure 5 highlights bed response at a high flow rate. Unlike previous two cases, pressure drop values in Figure 5(a), whether for pulsed or nonpulsed flow, are quite comparable. Now, sharp peaks in local pressure transients seen before at lower flow rates are missing.

Two features of Figures 3–5 are noteworthy. First, there is a significant difference in the local and global responses of the bed which are evident from pressure transients. The effect of flow pulsation is pronounced in local pressure transients, which in fact reflects the turbulence in the local solid motion. This is however not seen in the global pressure profiles as the local fluctuations in solid motion in different bed regions tend to cancel each other. Second, pulsation is more effective at lower velocities when fluctuations in solid motion due to the fluidizing velocity are rather small. Pulsed flow in this case greatly enhances the solid phase turbulence. When the fluidizing velocity is high, the solid phase turbulence is itself high. Therefore, the contribution of the additional solid turbulence generated by flow pulsation is relatively less apparent on the bed dynamics.

Figure 6 shows local pressure transients of 0.10 Hz pulsed fluidized bed at two different velocities. Since the minimum fluidization velocity for 0.10 Hz fluidization velocity is 28.3 mm/s [12], incipient fluidization conditions prevail at 33.2 mm/s, while the bed is completely fluidized at 134.8 mm/s. Two consecutive pulses are plotted together for each velocity. The agreement is excellent. For the case of 33.2 mm/s in Figure 6(a), there are several peaks and the peak pressure drop is higher due to greater disturbance in the bed as

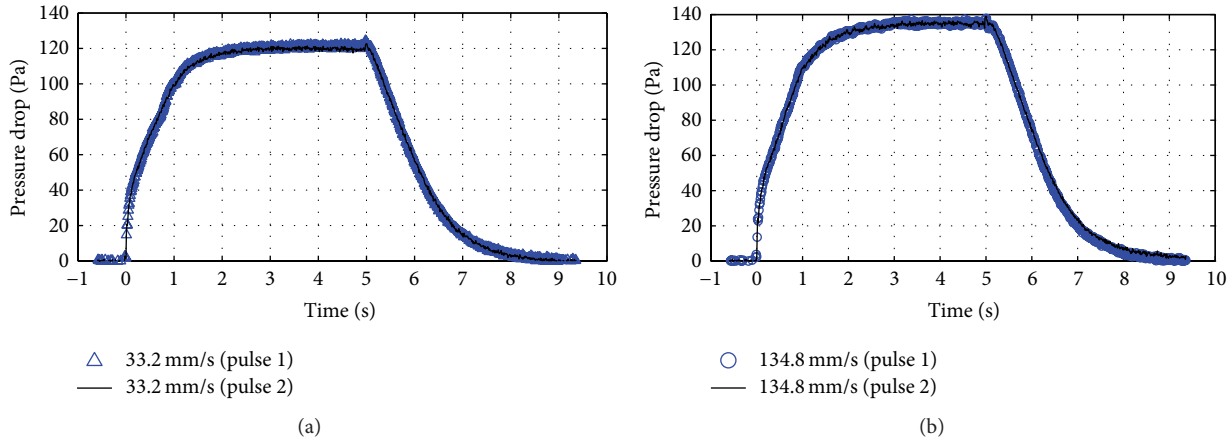


Figure 7: Global bed response for two consecutive pulses at 0.10 Hz at velocities: (a) 33.2 mm/s, (b) 134.8 mm/s.

compared to the case of higher velocity (134.8 mm/s) shown in Figure 6(b). There is a small decrease in the steady-state pressure drop at the higher velocity as compared to the one at the lower velocity. Moreover, the global minimum is relatively smaller (in magnitude) and delayed at the higher velocity. This is caused by the fact that solid mass between the two ports of the pressure transducer progressively decreases as the velocity increases owing to enhanced bed voidage. This lowers the pressure drop when the fluidized bed stabilizes after the valve opening and moreover leads to a relatively smaller solid phase momentum when the bed collapse process starts.

Figure 7 shows global pressure transients at two different velocities. There is once again excellent repeatability across the data for consecutive pulses in both cases. The duration of 5 seconds is just sufficient to allow the bed to attain steady state after the opening and closing of the flow. Though the air velocity is significantly different, the global bed response is almost identical except that the steady-state pressure drop is higher for 134.8 mm/s. The lower pressure drop at lower velocity is due to the incomplete fluidization of the agglomerated fluidized mass present in the lower region of the bed.

The pressure transient for the falling bed is shown in Figure 8 for 0.05 Hz pulsed fluidized bed at different air superficial velocities. As explained before, the steady-state pressure drop is a little lower for low velocities, most probably due to incomplete fluidization arising from bed nonhomogeneity. As the large agglomerates of nanopowder in the lower portion of the bed get fluidized, the pressure drop increases, ultimately reaching a constant value at higher velocities. When the air flow to the bed is cut off, pressure transients initially decrease linearly, but a rather slow exponential decrease is seen in the second stage of the bed collapse. The first stage is due to the free fall of the initially fluidized particles under gravity while the second stage is due to the filling up of void spaces by the fine particle in the bed as pointed out by Asif and Ali [18].

Figure 9 shows the transients of global pressure drop for 0.25 Hz pulsed fluidized bed. Unlike the previous case, pressure transients during the bed collapse here do not attain zero values. Owing to the high frequency, the bed did not

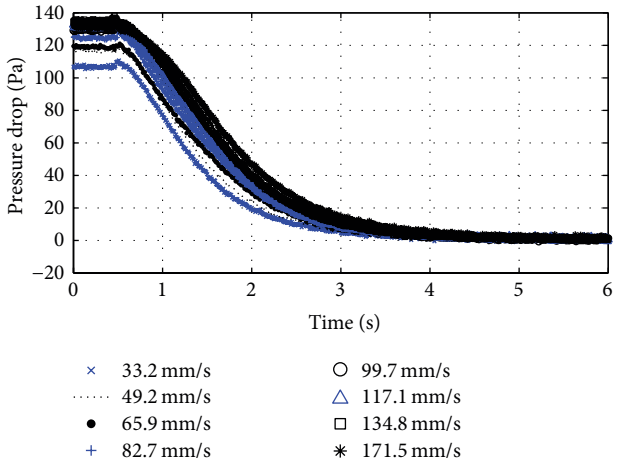


Figure 8: Global transients of falling bed at different fluid velocities for pulsation frequency of 0.05 Hz.

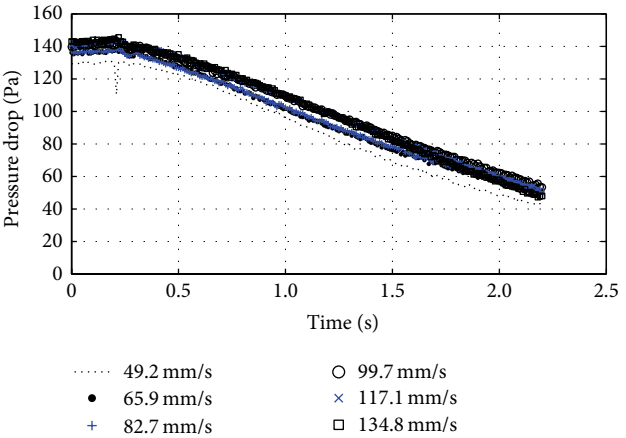


Figure 9: Global transients of falling bed at different fluid velocities for pulsation frequency of 0.25 Hz.

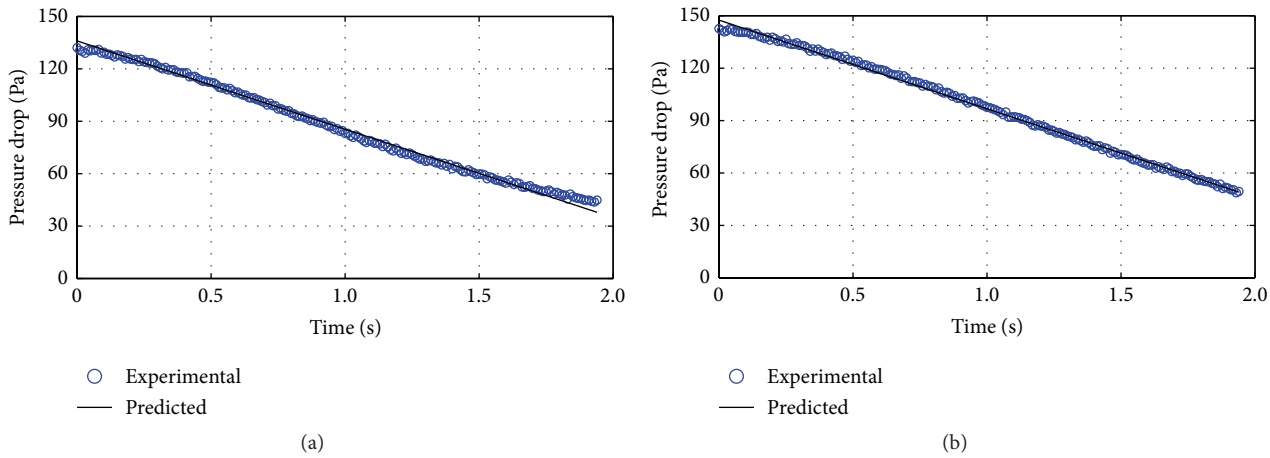


Figure 10: Comparison of predicted model and experimental data of the falling bed for 0.25 Hz pulsed flow at (a) 49.2 mm/s and (b) 134.8 mm/s.

get enough time to complete the process of the collapse. Therefore, only the linear fall of the bed is seen here and not the second stage of slower fall. As a result, the pressure drop does not attain zero values before the occurrence of the next pulse. Moreover, there is another rather subtle difference as far as 0.05 Hz and 0.25 Hz pulsed fluidized beds are concerned. A greater difference among the pressure transients at different velocities is visible in case of 0.05 Hz as compared to ones for 0.25 Hz. This is an indication that bed homogeneity is greater for pulsed fluidized bed with higher frequency.

In the present, the collapse stage of the pulsed fluidized bed was modelled here using the mathematical description presented earlier. Figures 10(a) and 10(b) show the experimental data along with model predictions for the case of 0.25 Hz frequency for two different flow rates. The slope of the global pressure transient was evaluated for different flow rates. From the slope of the bed transient profile, the particle terminal velocity was evaluated which yielded the value of the effective hydrodynamic diameter using (28). Effective averaged particle diameters, thus obtained, are reported in Table 1 for different velocities. Corresponding values of particle Reynolds number are also reported in the table. Low values of Reynolds number justify the use of Stokes law used for computing the particle diameter in (28). In all cases, $R^2$ values are greater than 0.99 which indicate an excellent agreement between the data and the model for all velocities. It is seen here that the effective hydrodynamic diameter remains almost constant irrespective of the air velocity except when the air velocity is low, that is, 49.2 mm/s. This may be attributed to bed nonhomogeneity along the height. The lower bed regions with larger agglomerates are not fully fluidized at lower velocities; the computed size is therefore bigger. As the velocity is increased, the bed turbulence owing to air flow also increases which results in smaller size of agglomerates.

The experimental data and the model fit for the 0.05 Hz pulsed fluidized bed are shown in Figures 11(a) and 11(b) for two different velocities. Only the linear portion of the experimental data which describes the fall of bed solids under the influence of gravity was considered for the model fit. The model agreement is seen to be excellent. The air velocity and the corresponding values of the Reynolds number, the goodness of fit, and the particle diameter are presented in Table 2. Fits are seen to be excellent which are evident from $R^2$ values. There appears to be a decrease, however small, in the effective diameter as the air velocity is increased.

Table 1: Computed average effective diameter of agglomerates and Reynolds number for 0.25 Hz pulsed fluidized bed.

| Velocity (mm/s) | $R^2$ | $d_P$ ($\mu$m) | $N_{\mathrm{Re}}$ (−/−) |
|---|---|---|---|
| 49.2 | 0.995 | 13.9 | 0.04 |
| 65.9 | 0.995 | 13.2 | 0.05 |
| 82.7 | 0.997 | 12.7 | 0.06 |
| 99.7 | 0.998 | 12.6 | 0.08 |
| 117.1 | 0.999 | 12.6 | 0.09 |
| 134.8 | 0.997 | 12.9 | 0.11 |

Results for all the three pulse frequencies are summarized in Figure 12 which includes the data reported earlier for the 0.10 Hz flow pulsation [18]. Unlike other two cases, hydrodynamic diameters at lower velocities in this case are a little less as compared to ones at higher velocities. This trend, however small in magnitude, points to a greater bed homogeneity of pulsed fluidized bed of 0.10 Hz frequency. It is worthwhile to mention that the steady fluidization condition yielded the effective diameter value to be 16.4 $\mu$m [12].

At this stage, instead of relying on the literature data reported earlier [12], we again carried out particle size analysis of the sample. The particle size distribution for three different runs and their mean are shown in Figure 13. The volume-mean diameters for the three runs were 20.68, 23.20, and 18.17 $\mu$m, with their mean value being 20.68 $\mu$m. Thus, due to flow pulsation, we obtain an almost 40% decrease in

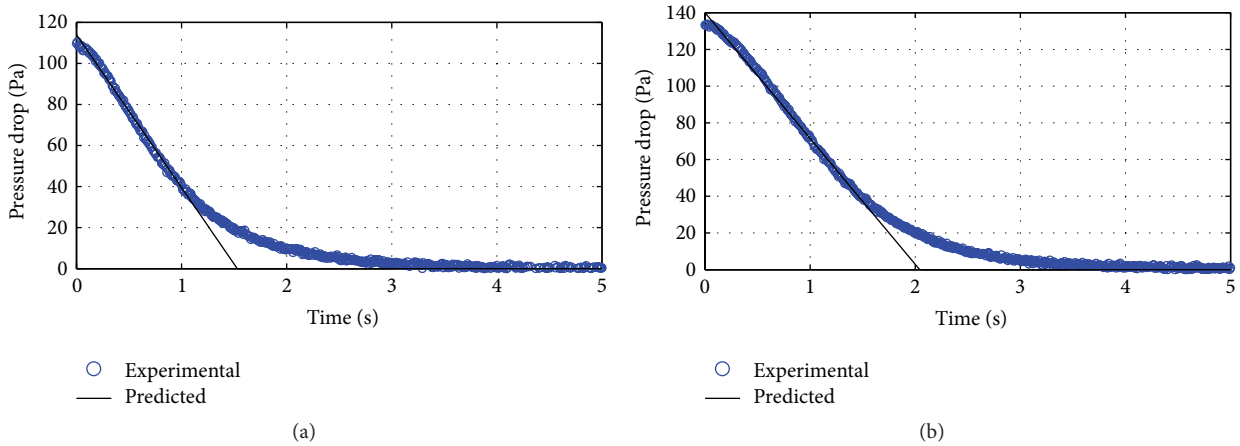


Figure 11: Comparison of predicted model and experimental data of the falling bed for 0.05 Hz pulsed flow at (a) 33.2 mm/s and (b) 134.8 mm/s.

Table 2: Computed average effective diameter of agglomerates and Reynolds number for 0.05 Hz pulsed fluidized bed.

| Velocity (mm/s) | $R^2$ | $d_P$ ($\mu$m) | $N_{Re}$ (−/−) |
|---|---|---|---|
| 33.2 | 0.995 | 13.8 | 0.03 |
| 49.2 | 0.995 | 13.7 | 0.05 |
| 65.9 | 0.993 | 13.2 | 0.06 |
| 82.7 | 0.992 | 13.4 | 0.08 |
| 99.7 | 0.996 | 13.2 | 0.10 |
| 117.1 | 0.995 | 13.0 | 0.11 |
| 134.8 | 0.997 | 12.9 | 0.13 |
| 171.5 | 0.995 | 12.4 | 0.16 |

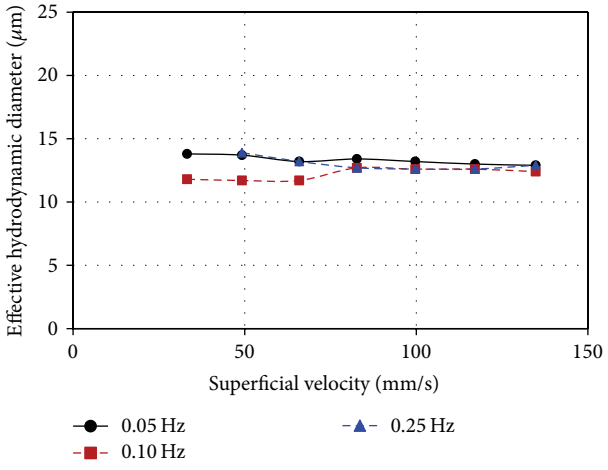


Figure 12: Effect of flow rate and the frequency on the effective hydrodynamic diameter of agglomerates.

the effective hydrodynamic diameter of agglomerates which vary in the range of 14 $\mu$m to 12.5 $\mu$m.

On the other hand, using the minimum fluidization velocity data, the mean particle diameter was calculated in the previous study [12]. The mean particle diameters for

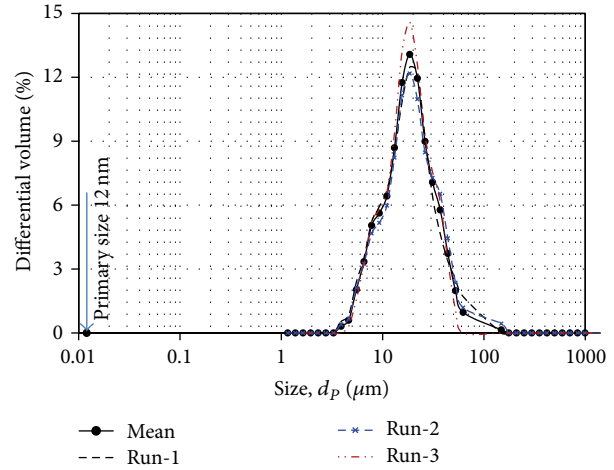


Figure 13: Particle size analysis of sample of nanopowder (Aerosil 200 with primary particle size of 12 nm).

frequencies 0.05 Hz, 0.10 Hz, and 0.25 Hz at the minimum fluidization velocity of 30.5 mm/s, 28.3 mm/s, and 41.1 mm/s were reported to be 10.0 $\mu$m, 8.9 $\mu$m, and 10.1 $\mu$m, respectively. These values are a little lower as compared to ones obtained here from the bed collapse data. This is in fact not surprising since the computation of the agglomerate size in the previous study [12] was based on the local pressure drop data when the pressure taps were located 112 mm and 230 mm above the distributor. This region excludes larger agglomerates often present near the distributor.

## 5. Conclusions

Flow pulsation clearly leads to deagglomeration, causing significant decreases in the agglomerate size. In the present case, there was an almost 40% size reduction. However, there is no clear evidence in the present investigation that pulse frequency affects the deagglomeration behavior. Similar results

were in fact obtained earlier from the incipient fluidization data. It is important to note here that the evaluation of particle terminal velocity here takes into account complete set of bed collapse data for each velocity unlike incipient fluidization data that depends upon the change of the slope of the velocity versus pressure drop profile, which is often quite unpredictable for ultrafine powders and is therefore more susceptible to error. It is interesting to note that the flow velocity also does not cause any appreciable effect on the agglomerate size even though it is normally expected that higher turbulence associated with higher velocity might lead to smaller agglomerates.

## Appendix

For the interface located at $L_1$, the fluid phase balance leads to

$$C_{g_1}\left(U_{g_1}-\frac{dL_1}{dt}\right)=C_{g_2}\left(U_{g_2}-\frac{dL_1}{dt}\right), \tag{A.1}$$

where $C_S$ denotes solid fraction and $U_S$ is its velocity. Rearranging,

$$\left(C_{g_1}-C_{g_2}\right)\frac{dL_1}{dt}=C_{g_1}U_{g_1}-C_{g_2}U_{g_2}. \tag{A.2}$$

Since $C_{g_0}=1$ owing to pure gas phase below the distributor and $U_{S_1}=0$, one can write

$$U_{g_0}=C_{g_1}U_{g_1}. \tag{A.3}$$

Therefore, (A.1) reduces to

$$\left(C_{g_1}-C_{g_2}\right)\frac{dL_1}{dt}=U_{g_0}-C_{g_2}U_{g_2}. \tag{A.4}$$

Since for Region 2 $U_{g_0}=C_{S_2}U_{S_2}+C_{g_2}U_{g_2}$ this relationship and the volume fraction constraint, when substituted into (A.4), yield (3).

For the interface located at $L_2$, the fluid phase balance leads to

$$\begin{aligned}C_{g_2}\left(U_{g_2}-\frac{dL_2}{dt}\right)&=C_{g_3}C_E\left(U_{g_3}-\frac{dL_2}{dt}\right)\\&\quad+C_{g_3}C_W\left(U_W-\frac{dL_2}{dt}\right)\\&\quad+C_B\left(U_B-\frac{dL_2}{dt}\right),\end{aligned} \tag{A.5}$$

where $C_B$, $C_E$, and $C_W$ are volumetric fractions of bubbles, emulsion phase, and wakes, respectively, in the region between $L_2$ and $L_3$, whereas $U_B$, $U_E$, and $U_W$ are their respective velocities. Here, bubbles consist of gas phase only while both gas and solid phases comprise wakes, having the same composition as the emulsion phase (Assumption 2).

Equation (A.5) can be rearranged as

$$\begin{aligned}&\left(C_{g_2}-C_{g_3}C_E-C_{g_3}C_W-C_B\right)\frac{dL_2}{dt}\\&\quad=C_{g_2}U_{g_2}-C_{g_3}C_EU_{g_3}-\left(C_{g_3}C_W+C_B\right)U_B.\end{aligned} \tag{A.6}$$

Note that emulsion phases of both regions, that is, Region 2 and Region 3, have the same composition (Assumption 3). Moreover, $U_W=U_B$ (Assumption 1). Using the relationships

$$\begin{aligned}C_B+C_E+C_W&=1,\\C_gU_g+C_SU_S&=U_E,\\C_BU_B+C_EU_E+C_WU_W&=U_{g_0},\end{aligned} \tag{A.7}$$

the above equation (A.6) can be simplified to

$$C_B\frac{dL_2}{dt}=U_{S_2}-C_EU_{S_3}-C_WU_B \tag{A.8}$$

which is basically (9).

One can similarly write for surface located at $L_3$

$$\begin{aligned}&C_{g_3}C_E\left(U_{g_3}-\frac{dL_3}{dt}\right)+C_{g_3}C_W\left(U_W-\frac{dL_3}{dt}\right)\\&\quad+C_B\left(U_B-\frac{dL_3}{dt}\right)=C_{g_4}\left(U_{g_4}-\frac{dL_3}{dt}\right),\end{aligned} \tag{A.9}$$

where the suffix "4" denotes the region above the fluidized bed. Since $L_3$ is the top fluidized bed interface, $C_{g_4}=1$ and $U_{g_4}=U_{g_0}$. Now, the above equation can be simplified to

$$\begin{aligned}&\left(1-C_{g_3}C_E-C_{g_3}C_W-C_B\right)\frac{dL_3}{dt}\\&\quad=U_{g_0}-C_{g_3}C_EU_{g_3}-\left(C_{g_3}C_W+C_B\right)U_B.\end{aligned} \tag{A.10}$$

Simplifying and rearranging (A.10) gives (15).

## Nomenclature

$C_B$: Fraction of bubbles (−/−)
$C_{S_i}$: Fraction of solid particles in the $i$th region (−/−)
$C_W$: Fraction of solid particles in wakes in region AB (−/−)
$d_P$: Effective hydrodynamic diameter of nanoparticle agglomerates (m)
$L_0$: Initial height of the bed at time $t=0$ (m)
$L_1$: Height of Region 1 (m)
$L_2$: Height of Region 2 (m)
$L_3$: Top bed interface (m)
$N_{\mathrm{Re}}$: Reynolds number $N_{\mathrm{Re}}=d_PU_{g_0}\rho_f/\mu$
$\Delta P$: Pressure drop (Pa)
$t_{b,\mathrm{end}}$: Time of bubble escape from the bed (s)
$t_{\mathrm{end}}$: Total time of collapse of bed (s)
$U_B$: Bubble velocity (m/s)
$U_E$: Emulsion phase velocity (m/s)
$U_{g_0}$: Gas superficial velocity (m/s)
$U_{g_i}$: Gas phase velocity in the $i$th region (m/s)
$U_r$: Particle relative (or slip) velocity with respect to the fluid (m/s)
$U_{S_i}$: Solid velocity of the $i$th region (m/s)
$U_t$: Particle terminal settling velocity (m/s)
$U_W$: Wake velocity (m/s).

*Greek Symbols*

$\alpha$: Parameter defined by (22)
$\beta$: Slope in (24) (Pa/s)
$\varepsilon$: Bed porosity (−/−)
$\gamma$: Parameter defined by (25)
$\mu$: Air viscosity (N·s $m^{-2}$)
$\rho_f$: Air density (kg/$m^3$)
$\rho_p$: True solid density (kg/$m^3$).

## Conflict of Interests

The authors declare no conflict of interests.

## Acknowledgment

Authors extend their appreciation to the Deanship of Scientific Research at King Saud University for funding this work through the Research Group Project no. RGP-VPP-292.

## References

[1] A. Akhavan, F. Rahman, S. Wang, and M. Rhodes, "Enhanced fluidization of nanoparticles with gas phase pulsation assistance," *Powder Technology*, vol. 284, pp. 521–529, 2015.

[2] H. Liu, L. Zhang, T. Chen, S. Wang, Z. Han, and S. Wu, "Experimental study on the fluidization behaviors of the superfine particles," *Chemical Engineering Journal*, vol. 262, pp. 579–587, 2015.

[3] X. Liang, H. Duan, T. Zhou, and J. Kong, "Fluidization behavior of binary mixtures of nanoparticles in vibro-fluidized bed," *Advanced Powder Technology*, vol. 25, no. 1, pp. 236–243, 2014.

[4] H. Duan, X. Liang, T. Zhou, J. Wang, and W. Tang, "Fluidization of mixed $SiO_2$ and ZnO nanoparticles by adding coarse particles," *Powder Technology*, vol. 267, pp. 315–321, 2014.

[5] L. F. G. De Souza, M. Nitz, P. A. Lima, and O. P. Taranto, "Drying of sodium acetate in a pulsed fluid bed dryer," *Chemical Engineering & Technology*, vol. 33, no. 12, pp. 2015–2020, 2010.

[6] A. Akhavan, J. R. van Ommen, J. Nijenhuis, X. S. Wang, M.-O. Coppens, and M. J. Rhodes, "Improved drying in a pulsation-assisted fluidized bed," *Industrial & Engineering Chemistry Research*, vol. 48, no. 1, pp. 302–309, 2009.

[7] F. C. Godoi, N. R. Pereira, and S. C. S. Rocha, "Analysis of the drying process of a biopolymer (poly-hydroxybutyrate) in rotating-pulsed fluidized bed," *Chemical Engineering and Processing: Process Intensification*, vol. 50, no. 7, pp. 623–629, 2011.

[8] A. Reyes, A. Mahn, C. Guzmán, and D. Antoniz, "Analysis of the drying of broccoli florets in a fluidized pulsed bed," *Drying Technology*, vol. 30, no. 11-12, pp. 1368–1376, 2012.

[9] A. Akhavan, F. Rahman, X. S. Wang, and M. J. Rhodes, "Assisted fluidization of nanoparticles through gas-phase pulsation," in *Proceedings of the 35th Australasian Chemical Engineering Conference (CHEMECA '07)*, pp. 1909–1916, Melbourne, Australia, September 2007.

[10] A. Jelic, C. Cruz-Morató, E. Marco-Urrea et al., "Degradation of carbamazepine by Trametes versicolor in an air pulsed fluidized bed bioreactor and identification of intermediates," *Water Research*, vol. 46, no. 4, pp. 955–964, 2012.

[11] H. Khosravi Bizhaem and H. Basirat Tabrizi, "Experimental study on hydrodynamic characteristics of gas–solid pulsed fluidized bed," *Powder Technology*, vol. 237, pp. 14–23, 2013.

[12] S. S. Ali and M. Asif, "Fluidization of nano-powders: effect of flow pulsation," *Powder Technology*, vol. 225, pp. 86–92, 2012.

[13] S. S. Ali, M. Asif, and A. Ajbar, "Bed collapse behavior of pulsed fluidized beds of nano-powder," *Advanced Powder Technology*, vol. 25, no. 1, pp. 331–337, 2014.

[14] Y. Nie and D. Liu, "Dynamics of collapsing fluidized beds and its application in the simulation of pulsed fluidized beds," *Powder Technology*, vol. 99, no. 2, pp. 132–139, 1998.

[15] J. F. Richardson and W. N. Zaki, "Sedimentation and fluidisation: part I," *Chemical Engineering Research and Design*, vol. 75, supplement, pp. S82–S100, 1997.

[16] R. B. Bird, W. E. Stewart, and E. N. Lightfoot, *Transport Phenomena*, John Wiley & Sons, New York, NY, USA, 2nd edition, 2007.

[17] P. Cherntongchai, T. Innan, and S. Brandani, "Mathematical description of pressure drop profile for the 1-valve and 2-valve bed collapse experiment," *Chemical Engineering Science*, vol. 66, no. 5, pp. 973–981, 2011.

[18] M. Asif and S. S. Ali, "Bed collapse dynamics of fluidized beds of nano-powder," *Advanced Powder Technology*, vol. 24, no. 6, pp. 939–946, 2013.